nanomaterials

MDPI

Article

Rheological Modeling of Metallic Oxide Nanoparticles Containing Non-Newtonian Nanofluids and Potential Investigation of Heat and Mass Flow Characteristics

Muhammad Rizwan [1], Mohsan Hassan [1], Oluwole Daniel Makinde [2], Muhammad Mubashir Bhatti [3,*] and Marin Marin [4]

[1] Department of Mathematics, COMSATS University Islamabad, Lahore Campus, Lahore 54000, Pakistan; m.rizwan7571@gmail.com (M.R.); mohsan.hassan@cuilahore.edu.pk (M.H.)
[2] Faculty of Military Science, Stellenbosch University, Private Bag X2, Saldanha 7395, South Africa; makinded@gmail.com
[3] College of Mathematics and Systems Science, Shandong University of Science and Technology, Qingdao 266590, China
[4] Department of Mathematics and Computer Science, Transilvania University of Brasov, 500036 Brasov, Romania; m.marin@unitbv.ro
* Correspondence: mmbhatti@sdust.edu.cn or mubashirme@hotmail.com

Abstract: Nanofluids have great potential due to their improved properties that make them useful for addressing various industrial and engineering problems. In order to use nanofluids on an industrial scale, it is first important to discuss their rheological behavior in relation to heat transfer aspects. In the current study, the flow characteristics of nanofluids are discussed using a mathematical model that is developed by fundamental laws and experimental data. The data are collected in the form of viscosity versus shear rate for different homogeneous ethylene glycol- (EG) based nanofluids, which are synthesized by dispersing 5–20% nanoparticle concentrations of SiO_2, MgO, and TiO_2 with diameters of (20–30 nm, 60–70 nm), (20 nm, 40 nm), and (30 nm, 50 nm), respectively. The data are fitted into a rheological power-law model and further used to govern equations of a physical problem. The problem is simplified into ordinary differential equations by using a boundary layer and similarity transformations and then solved through the numerical Runge–Kutta (RK) method. The obtained results in the form of velocity and temperature profiles at different nanoparticle concentrations and diameters are displayed graphically for discussion. Furthermore, displacement and momentum thicknesses are computed numerically to explain boundary-layer growth. The results show that the velocity profile is reduced and the temperature profile is raised by increasing the nanoparticle concentration. Conversely, the velocity profile is increased and the temperature profile is decreased by increasing the nanoparticle diameter. The results of the present investigation regarding heat and mass flow behavior will help engineers design equipment and improve the efficacy and economy of the overall process in the industry.

Keywords: non-Newtonian nanofluids; mathematical modeling based on experimental data; heat-flow characteristics; power-law fluid model

Citation: Rizwan, M.; Hassan, M.; Makinde, O.D.; Bhatti, M.M.; Marin, M. Rheological Modeling of Metallic Oxide Nanoparticles Containing Non-Newtonian Nanofluids and Potential Investigation of Heat and Mass Flow Characteristics. *Nanomaterials* **2022**, *12*, 1237. https://doi.org/10.3390/nano12071237

Academic Editor: Mikhail Sheremet

Received: 10 March 2022
Accepted: 4 April 2022
Published: 6 April 2022

1. Introduction

Nanofluids are advanced classes of heat-transfer fluids designed by diffusing nanometer-scale particles of metal, metal oxide, carbon nanotubes, nitride, carbide, and compound materials in traditional base fluids such as ethylene glycol (EG), water, oils, etc. [1–4]. As a consequence of the improved properties related to heat transfer and chemical stability [5–8], nanofluids have become immensely attractive and demonstrate several potential applications in many fields relating to solar collection, transportation, the energy industry, refrigeration, the cooling process, chemistry, biomedicine, and the environment [8–15].

Many studies are reported in the literature on the different properties of nanofluids, such as density, thermal conductivity, viscosity, specific heat, etc. [16–20]. However, it is observed that the most critical properties of nanofluids are their rheological properties. For example, based on the different types of base fluids, the nanofluids containing MWCNTs exhibit both Newtonian and non-Newtonian behavior. The composition of MWCNTs with water, resin, and oil displays non-Newtonian behavior [21–30]. Normally, nanofluids consisting of MWCNTs reveal Newtonian behavior at low volume fractions and non-Newtonian behavior at high volume fractions [21,22]. In the case of TiO_2-water nanofluids, the fluids mostly exhibit non-Newtonian behavior [31–34]. Contrarily, Bobbo et al. [35] and Penkavova et al. [36] reported that, for all compositions, TiO_2/water nanofluids displayed Newtonian behavior. In the case of SiO_2, the nanofluids with different base fluids showed behavior that was close to Newtonian behavior [37–42]. In short, the nanofluids exhibited non-Newtonian behavior [43–47] in many cases, whereas few showed Newtonian behavior [35,36,48].

Non-Newtonian nanofluids that were synthesized by water or EG revealed shear-thinning behavior [43–47]. Shear-thinning fluid is a kind of non-Newtonian fluid wherein viscosity declines by the rise of the shear rate. There are several mathematical models in the literature used to investigate the rheological behavior of such fluids. In the list of models, the power-law model demonstrates the relation between viscosity and shear rate. It is very popular in various disciplines, such as the biosciences and food and processing reservoir engineering [6–14]. Specifically, it is widely used in fluid flow problems under different conditions, and it is even used as a working principle in different kinds of rheometers.

In previous numerical studies, a deficiency was found in the theoretical models that can guess the exact behavior of nanofluids. The researchers used the Newtonian model for homogeneous nanofluids, which does not apply to the experimental behavior of all cases. No one study is available where homogeneous nanofluids deal with the non-Newtonian model. In the current study, we used a non-Newtonian power-law fluid model according to the trend of an experimental study. The parameters of the model are expressed as the function of nanoparticles, and we developed new mathematical relations to these parameters. By using these relations that govern equations, the physical problem became complex because every parameter is a function of the volume fraction, and solving this problem is not easy.

In this study, our goal is to investigate the flow behavior of non-Newtonian nanofluids, which are synthesized by the dispersion of metallic oxides in EG. For the flow, wedge shape is adopted as the geometry for our problem, which is favorable for accelerating or decelerating the fluids. The mathematical problem for flow is developed by the fundamental equations of fluid mechanics and modifies its parameters in view of the experimental evidence. The results from these equations are obtained in the form of velocity and temperature profiles and displayed in graphical form for discussion.

2. Nanofluid Modeling

In this section, the mathematical models of physical properties are developed by using experimental data for three homogenous nanofluids: SiO_2-EG, MgO-EG, and TiO_2-EG. The experimental data for nanofluids, which contain 5%, 10%, 15%, and 20% nanoparticle concentrations and (20–30 nm, 60–70 nm), (30 nm, 50 nm), and (20 nm, 40 nm) nanoparticle diameters, respectively, are collected for the study [1]. We have chosen the nanoparticles of materials SiO_2, MgO, and TiO_2 for the nanofluid because these materials are used in manufacturing on a large scale at industry level. EG is used as a base fluid because it can be utilized within sufficiently large temperature ranges. For rheological behavior, the power-law equation is applied for nanofluid modeling in the formation of the viscosity–shear rate relationship as follows [49]:

$$\mu(\dot{\gamma}) = \mu_{nf}\dot{\gamma}^{n-1} \quad (1)$$

where μ_{nf} is named as the consistency coefficient and n is the power index, which is justifiable according to the Newtonian or non-Newtonian behavior of fluids. When $n = 1$,

the fluid exhibits Newtonian behavior, and the fluid shows shear-thinning behavior when $n < 1$. The rheological behavior of said nanofluids at different nanoparticle concentrations is displayed in Figures 1–3.

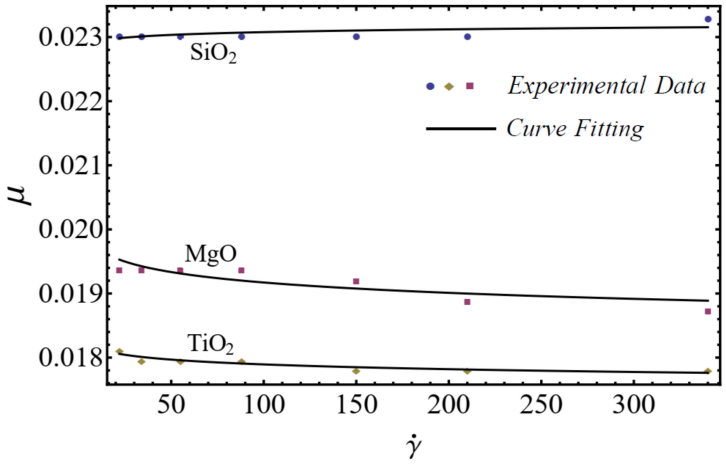

Figure 1. Experimental and mathematical rheological behavior of SiO_2-EG, MgO-EG, and TiO_2-EG nanofluids at 5% particle concentration.

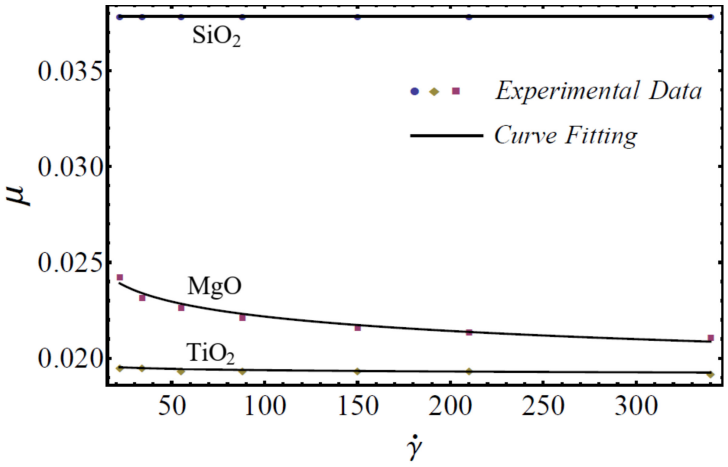

Figure 2. Experimental and mathematical rheological behavior of SiO_2-EG, MgO-EG, and TiO_2-EG nanofluids at 10% particle concentration.

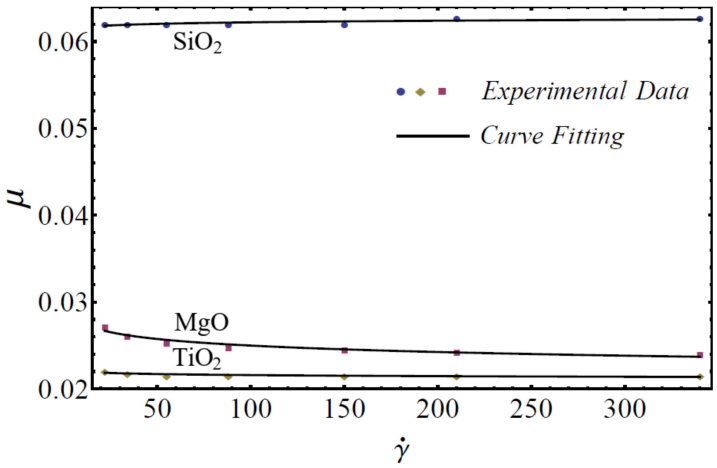

Figure 3. Experimental and mathematical rheological behavior of SiO_2-EG, MgO-EG, and TiO_2-EG nanofluids at 15% particle concentration.

The curve-fitting technique is used to calculate the values of the two empirical parameters $\left(\mu_{nf}\right)$ and (n) of Equation (1) for different nanofluids at different nanoparticle concentrations. For the curve fitting, we used the FindFit package from Mathematica, which is used for fitting in non-linear models. Afterward, these parameters are expressed in a second-order polynomial of the nanoparticle concentration ϕ. The equation of the power-law index and consistency index is defined as follows:

$$\left.\begin{array}{c} n = 1 + A_1\phi + A_2\phi^2 \\ \mu_{nf} = \left(1 + B_1\phi + B_2\phi^2\right)\mu_{bf} \end{array}\right\} \quad (2)$$

where A_1, A_2, B_1, and B_2 are constants calculated by using the curve-fitting technique in Table 1.

Table 1. The values of A_1, A_2, B_1, and B_2 for different nanofluids at different particle diameters.

	SiO_2-EG Nanofluid		**MgO-EG Nanofluid**		**TiO_2-EG Nanofluid**	
$d(nm) \rightarrow$	20–30	60–70	20	40	30	50
A_1	0.025	−0.04	−0.617	−0.0037	1.08	−0.013
A_2	−0.042	0.104	2.19	−0.112	12.63	−0.17
B_1	−4.8	−4.2	6.9	1.53	1.08	0.49
B_2	172.59	160.6	5.02	2.9	12.6	12.2

A good agreement is found between the calculated values and the polynomial equations, as seen in Figures 4 and 5.

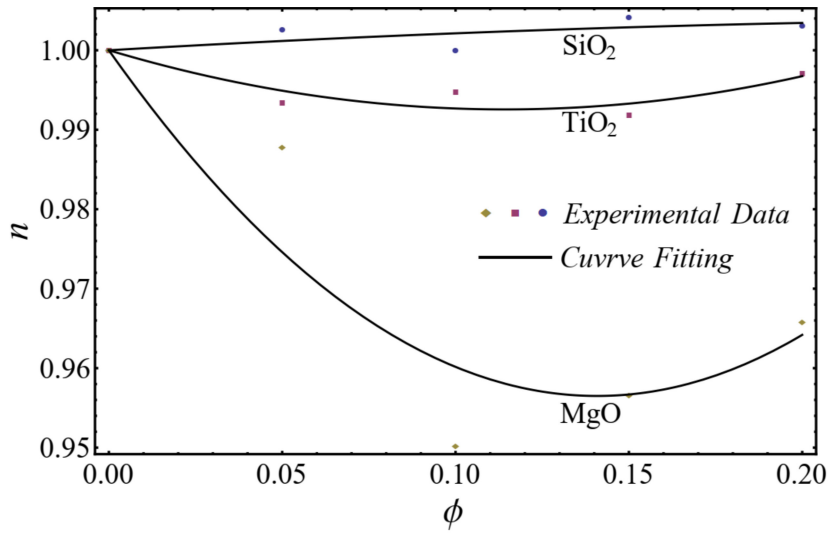

Figure 4. Curve fitting with experimental data for power-law index by using Equation (2).

Therefore, the viscosity model of Equation (1) is written as

$$\frac{\mu}{\mu_{bf}} = \left(1 + B_1\phi + B_2\phi^2\right)\dot{\gamma}^{1+A_1\phi+A_2\phi^2} \quad (3)$$

The co-relation models for other physical properties, such as heat capacitance $\left(\rho C_p\right)_{nf}$, effective density $\left(\rho_{nf}\right)$, and thermal conductivity $\left(k_{nf}\right)$, are defined by [50].

$$\rho_{nf} = \phi\,\rho_{np} + (1 - \phi\,)\rho_{bf} \quad (4)$$

$$\left(\rho C_p\right)_{nf} = \phi\left(\rho C_p\right)_{np} + (1 - \phi\,)\rho_{bf} \quad (5)$$

$$k_{nf} = \frac{k_{pe} + 2k_{bf} + 2\left(k_{pe} - k_{bf}\right)(1+\beta^*)^3\phi}{k_{pe} + 2k_{bf} - \left(k_{pe} - k_{bf}\right)(1+\beta^*)^3\phi} k_{bf} \tag{6}$$

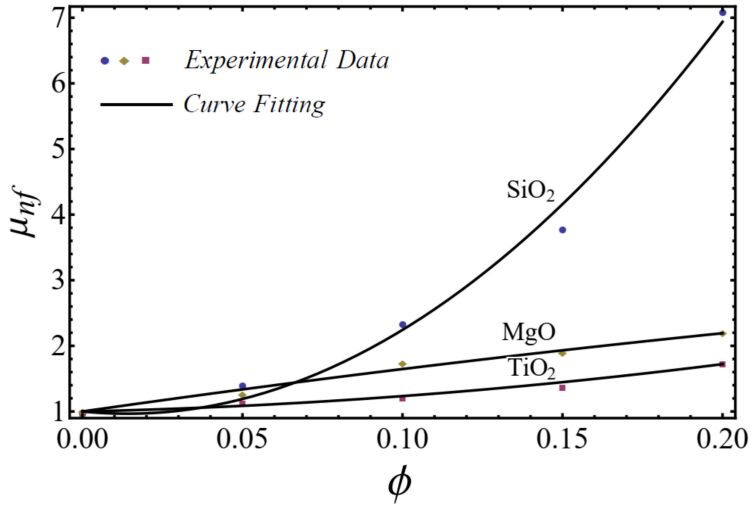

Figure 5. Curve fitting with experimental data for consistency index by using Equation (2).

In the above equations, the thermal conductivity of nanoparticle k_{npl} with a layer around the particle is defined by

$$k_{pe} = \frac{\left[2(1-\gamma) + (1+\beta^*)^3(1+2\gamma^*)\right]\gamma^*}{-(1-\gamma^*) + (1+\beta^*)^3(1+2\gamma^*)} k_{np} \tag{7}$$

where $\gamma^* = k_{layer}/k_{np}$ is the ratio of the layers of the nanoparticle to the thermal conductivities of the nanoparticle and $\beta^* = h_{layer}/R_p$ is the ratio of the layer's height to the radius of the nanoparticle.

3. Flow Modeling

We considered the boundary-layer fluid flow of nanofluids over a moving wedge, which has incompressible and steady-state properties. The wedge is moved with the velocity $u_w(x) = cx^m$, whereas $u_\infty(x) = bx^m$ is the velocity of the nanofluid over an inviscid region, as shown in Figure 6.

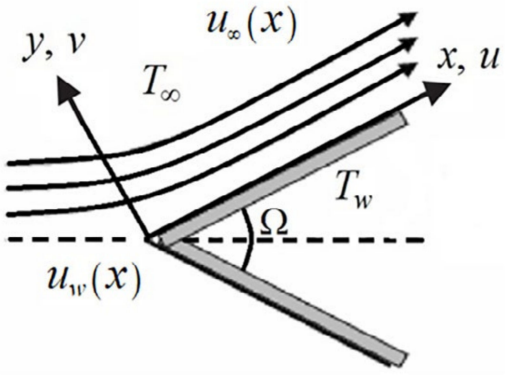

Figure 6. Structure of the flow.

On the basis of the results in Figures 1–3, the power-law model is used in momentum Equation (9). Under the boundary-layer approximation, the continuity, momentum, and energy equations are written as [51,52]

$$u_x + v_y = 0 \tag{8}$$

$$\rho_{nf}\left(u\,u_x + v\,u_y\right) = -\partial_x(p_e) + \mu_{nf}\,\partial_y\left(\left|u_y\right|^{n-1}u_y\right) \tag{9}$$

$$\left(\rho C_p\right)_{nf}\left(u\,T_x + v\,T_y\right) = k_{nf}\,\partial_y(T_y) \tag{10}$$

subjected to the boundary conditions

$$\left.\begin{array}{l} u(x,0) = -u_w(x),\ v(x,0) = 0, T(x,0) = T_w \\ u(x,\infty) = u_\infty(x), T(x,\infty) = T_\infty \end{array}\right\} \tag{11}$$

In the above equations, u and v are the velocity component parts in x and y directions. T_w is the temperature on the wedge's surface, and T_∞ is the temperature away from the surface $(T_w > T_\infty)$.

The relationship between the Falkner–Skan power-law parameter (m) and the wedge's angle $\beta = \Omega/\pi$ is stated as

$$m = \frac{\beta}{2-\beta} \tag{12}$$

For simplicity, we introduced the similarity transformations as follows:

$$\left.\begin{array}{l} \eta = \frac{y}{x}(\mathrm{Re}_x)^{\frac{1}{1+n}},\ \psi = u_\infty x(\mathrm{Re}_x)^{\frac{-1}{1+n}} f(\eta), \\ \theta(\eta) = \frac{T-T_\infty}{T_w-T_\infty},\ u = \frac{\partial\psi}{\partial x}, v = -\frac{\partial\psi}{\partial y} \end{array}\right\} \tag{13}$$

Substituting Equation (14) into Equations (9)–(12), we obtain the following equations:

$$n\frac{\mu_{nf}}{\mu_{bf}}\left(\left|f''\right|^{n-1}f'''\right) + \frac{\rho_{nf}}{\rho_{bf}}\left[\left(\frac{m(2n-1)+1}{(n+1)(m+1)}\right)ff''\frac{m}{m+1}f\prime^2\right] + \frac{m}{m+1} = 0 \tag{14}$$

$$\frac{k_{nf}}{k_{bf}}\theta'' + \mathrm{Pr}\frac{\left(\rho C_p\right)_{nf}}{\left(\rho C_p\right)_{bf}}\left(\frac{m(2n-1)+1}{(n+1)(m+1)}\right)f\theta\prime = 0 \tag{15}$$

with the boundary conditions

$$\left.\begin{array}{c} f(0) = 0, f\prime(0) = -\lambda,\ \theta(0) = 1, \\ \theta(\infty) = 0,\ f\prime(\infty) = 1, \end{array}\right\} \tag{16}$$

Here, the modified Prandtl number is $\mathrm{Pr}_x = \frac{\rho_{bf}c_{pbf}u_\infty x}{k_{bf}(\mathrm{Re}_x)^{\frac{2}{n-1}}}$, and the Reynold number is $\mathrm{Re}_x = (m+1)\frac{u_\infty^{2-n}x^n}{\nu_{bf}}$ and $\lambda = \frac{u_w}{u_\infty}$ velocities ratio.

4. Physical Parameters

4.1. Displacement Thickness

Displacement thickness is recognized as the vertical distance that is produced by the absent mass flow rate due to the boundary-layer phenomena. The expression for displacement thickness is written as

$$\delta^* = \int_0^\infty \left(1 - \frac{u}{u_\infty}\right)dy \tag{17}$$

Dimensionless displacement thickness is composed as

$$\delta^* = x(\mathrm{Re}_x)^{\frac{-1}{1+n}} \int_0^\infty (1 - f')d\eta \tag{18}$$

4.2. Momentum Thickness

Momentum thickness is the height of an imaginary stream, which is transmitted by the loss of the momentum flow rate due to the boundary-layer phenomena and is described mathematically as

$$\delta^{**} = \int_0^\infty \frac{u}{u_\infty}\left(1 - \frac{u}{u_\infty}\right)dy \tag{19}$$

Dimensionless momentum thickness is illustrated as

$$\delta^{**} = x(\mathrm{Re}_x)^{\frac{-1}{1+n}} \int_0^\infty f'(1 - f')d\eta \tag{20}$$

4.3. Skin Friction

The skin-friction coefficient is a dimensionless parameter that represents the shear stress at the wall. It is expressed as

$$C_f = \frac{\tau_w}{\frac{1}{2}\rho_{bf}{u_\infty}^2} \tag{21}$$

The wall shear stress τ_w can be written as

$$\tau_w = \mu\, u_y\big|_{y=0} \tag{22}$$

After applying transformation Equation (13), we receive

$$C_f = 2(m+1)(\mathrm{Re}_x)^{\frac{-1}{1+n}} \frac{\mu_{nf}}{\mu_{bf}} |f''(0)|^n \tag{23}$$

4.4. Nusselt Number

The Nusselt number is a dimensionless parameter that represents the convective heat-transfer rate at the wall. It is written in the following form:

$$Nu_x = \frac{hx}{k_{bf}} \tag{24}$$

Here, h is a convective heat-transfer coefficient that can be written as

$$h = -\frac{k_{nf}\ \partial_y(T - T_\infty)\big|_{y=0}}{(T_w - T_\infty)} \tag{25}$$

After applying transformation Equation (13), it is written as

$$Nu_x = -(\mathrm{Re}_x)^{\frac{1}{n+1}} \frac{k_{nf}}{k_{bf}}\theta'(0), \tag{26}$$

5. Solution Technique

The solution of Equations (14) and (15) with respect to Equation (16) is obtained by using the RK method. The method is executed in the following manner:

Let $f = F_1$, $\theta = G_1$, and convert Equations (14) and (15) into a system of first-order differential equations as

$$\left.\begin{array}{l} F_1\prime = F_2 \\ F_2\prime = F_3 \\ F_3\prime = \dfrac{\frac{\rho_{nf}}{\rho_{bf}}\left[\frac{m}{m+1}F_2{}^2 - \left(\frac{m(2n-1)+1}{(n+1)(m+1)}\right)F_1F_3\right] - \frac{m}{m+1}}{n\frac{\mu_{nf}}{\mu_{bf}}|F_3|^{n-1}} \\ G_1\prime = G_2 \\ G_2\prime = -\mathrm{Pr}\dfrac{k_{bf}}{k_{nf}}\dfrac{(\rho C_p)_{nf}}{(\rho C_p)_{bf}}\left(\frac{m(2n-1)+1}{(n+1)(m+1)}\right)F_1G_2 \end{array}\right\} \quad (27)$$

along the initial conditions

$$\left.\begin{array}{c} F_1(0) = 0, \\ F_2(0) = -\lambda, \\ F_3(0) = \Omega_1 \\ G_1(0) = 1 \\ G_2(0) = \Omega_2 \end{array}\right\} \quad (28)$$

Here Ω_1 and Ω_2 represent unknown boundary conditions.

To evaluate the accuracy of the results, the values of $f''(0)$ and $-\theta'(0)$ against the parameters of β and Pr are compared with the existing limited results [53,54] in Tables 2 and 3.

Table 2. Comparison of results for $f''(0)$ with numerical results in [53] when $\phi = 0$ and $n = 1$.

β	Present	[53]
0	0.46961	0.4696
1	0.92773	0.9277
2	1.23262	1.2326

Table 3. Comparison of results for $-\theta'(0)$ with numerical results in [54] when $\phi = 0$ and $\beta = 1$.

Pr	Present	[54]
1	0.57052	0.5705
2	0.74370	0.7437
6	1.11471	1.1147

6. Result and Discussion

In this segment, the results under the influence of the governing parameters are displayed for discussion. The first set of results is displayed graphically in the form of velocity and temperature profiles related to three homogenous metallic oxide nanofluids under the impacts of different nanoparticle concentrations and diameters. To see the effects of these parameters, the values of the geometry's parameters, for example, wedge angle $\Omega = \pi/6$, wedge speed $u_w = 0.01$, and free-stream velocity $u_\infty = 0.04$, are taken as fixed, and other parameters, such as the Reynold number and the modified Prandtl number, are varied according to different nanoparticle concentrations and diameters, which are listed in Tables 4 and 5. It is seen that the Reynold number is varied due to the variation in inertial force. The inertial force is a function of the power-law index, which becomes less than unity when the nanoparticle concentration is increased in the case of the MgO -EG and TiO_2-EG nanofluids. The modified Prandtl number is a function of the Reynold number and is varied by it.

Table 4. The values of Pr_x and Re_x numbers at different nanoparticle concentrations.

		SiO_2-EG Nanofluid D = 20−30 nm			MgO-EG Nanofluid D = 20 nm			TiO_2-EG Nanofluid D = 30 nm		
$\frac{\phi\rightarrow}{x\downarrow}$		5%	10%	15%	5%	10%	15%	5%	10%	15%
Pr_x	2	139.5	139.6	139.6	137.9	137.0	136.8	69.7	69.7	138.2
	4	139.5	139.5	139.5	139.1	138.9	138.8	139.4	139.0	278.1
Re_x	2	6045	6067	6085	5448	5149	5079	5898	5867	5851
	4	12,098	12,153	12,195	10,705	10,017	9858	11755	11,635	11,667

Table 5. The values of Pr_x and Re_x numbers at different nanoparticle diameters.

		SiO_2-EG Nanofluid		MgO -EG Nanofluid		TiO_2-EG Nanofluid	
$\frac{D(\mathrm{nm})\rightarrow}{x\downarrow}$		20–30	60–70	30	50	20	40
Pr_x	2	139.6	139.2	137.0	139.4	69.7	139.3
	4	139.5	278.5	138.9	278.7	139.0	278.5
Re_x	2	6067	5941	5149	5982	5847	5946
	4	12,153	11,855	10,017	11,951	11,635	11,866

6.1. Velocity Profiles

The results of the velocity profiles for the SiO_2-EG, MgO-EG, and TiO_2-EG nanofluids under the impact of distinct nanoparticle concentrations are illustrated in Figures 7–9. It is seen that the velocity profile for all specified nanofluids is reduced with the increase in nanoparticle concentration. In the current situation, the viscosity of present nanofluids is enhanced due to the increase in nanoparticle concentration, which causes the reduction in velocity. The trend of viscosity and velocity profile for the current study is found to be similar in existing studies [1,55–60]. These graphs assert that the dominant effects are found in the velocity profile of the SiO_2-EG nanofluid due to maximum viscosity as compared with the MgO-EG and TiO_2-EG nanofluids.

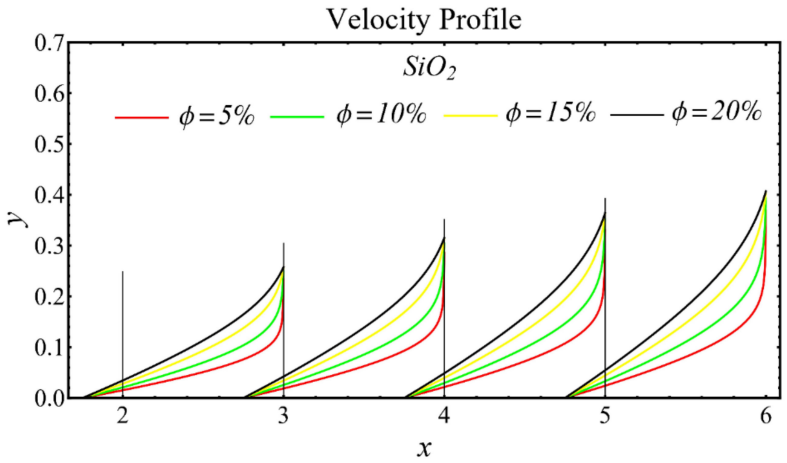

Figure 7. Velocity profile of SiO_2-EG nanofluid under influence of nanoparticle concentration.

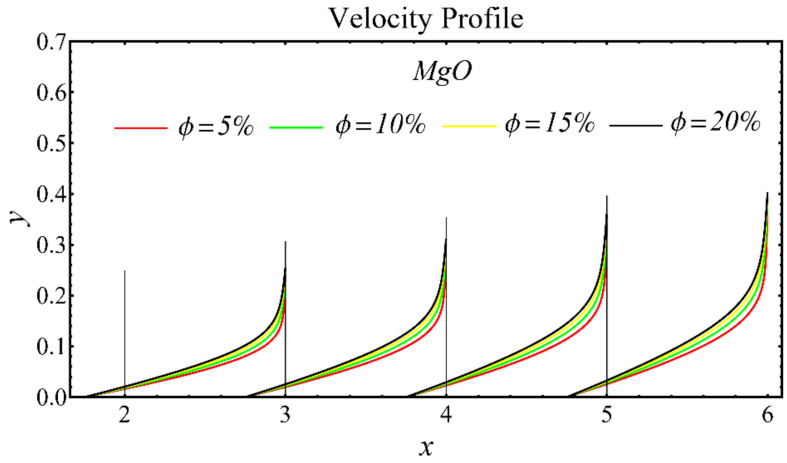

Figure 8. Velocity profile of MgO-EG nanofluid under influence of nanoparticle concentration.

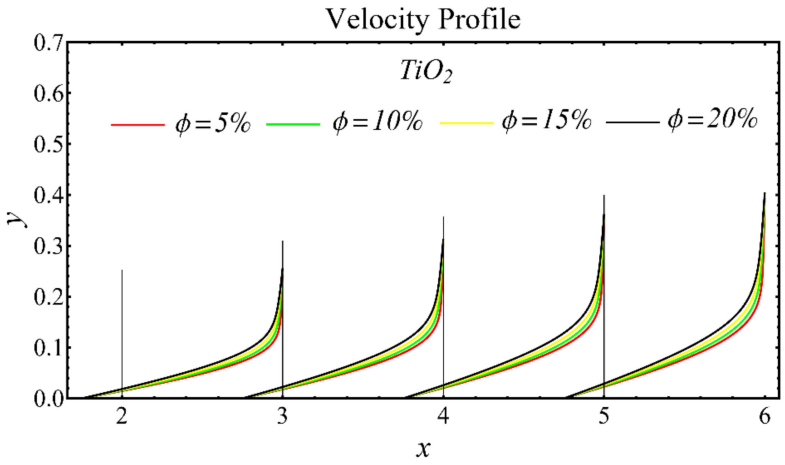

Figure 9. Velocity profile of TiO_2-EG nanofluid under influence of nanoparticle concentration.

The velocity profiles of the schematic nanofluids under the effect of two distinct nanoparticle diameters are shown in Figures 10–12. It is clear that the velocity profile is increased by increasing the nanoparticle diameter due to the decline in the viscosity of the nanofluids. In addition, the dominant impact of this parameter on the profile is found to be more pronounced in the MgO-EG nanofluid than in the other nanofluids.

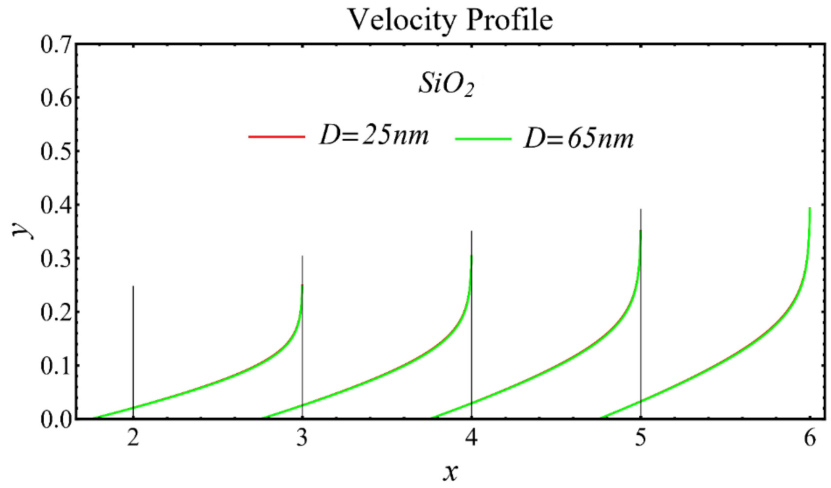

Figure 10. Velocity profile of SiO_2-EG nanofluid under influence of nanoparticle diameter.

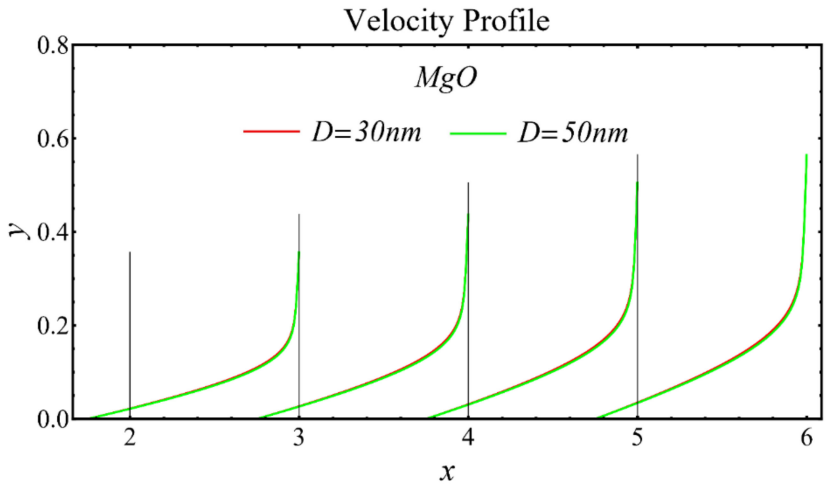

Figure 11. Velocity profile of MgO-EG nanofluid under influence of nanoparticle diameter.

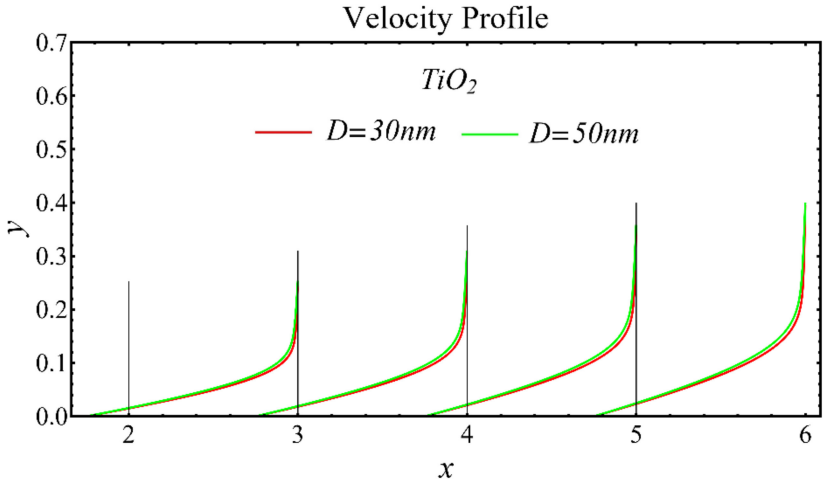

Figure 12. Velocity profile of TiO_2-EG nanofluid under influence of nanoparticle diameter.

6.2. Temperature Profiles

The graphs of the temperature profiles for the nanofluids with respect to various nanoparticle concentrations are displayed in Figures 13–15. The figures show that the temperature is raised with the increase in nanoparticle concentration. The fact is that the temperature distribution is enhanced due to the increase in thermal conductivity and the decline in specific heat. The trend of this profile is also matched with the trend demonstrated in existing studies [55–60]. Moreover, the graphs disclose that the temperature of the SiO_2-EG nanofluid is extensively affected by the enhancement of nanoparticle concentrations as compared with the other nanofluids.

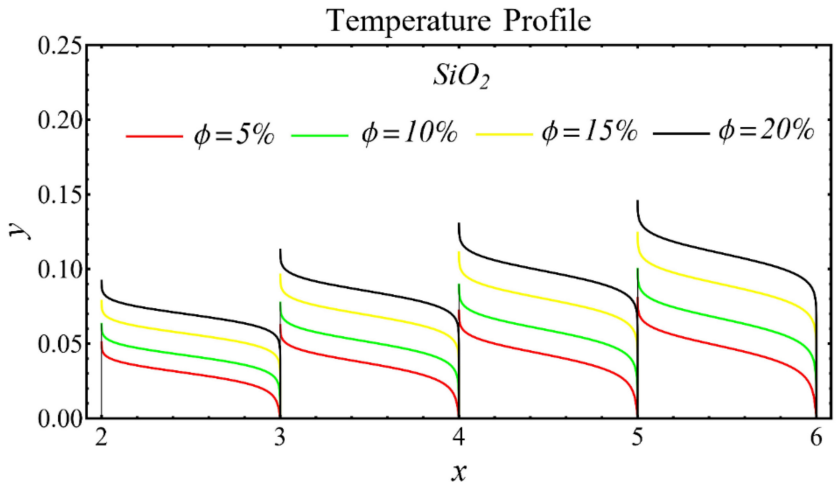

Figure 13. Temperature profile of SiO_2-EG nanofluid under influence of nanoparticle concentration.

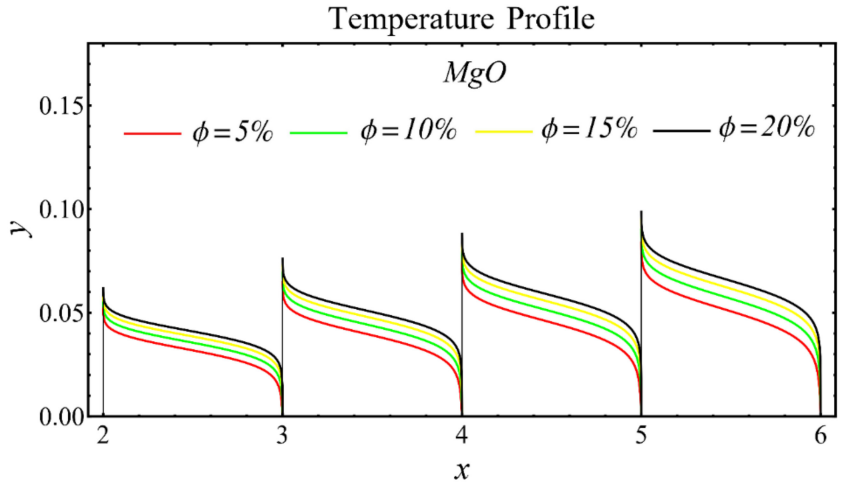

Figure 14. Temperature profile of MgO-EG nanofluid under influence of nanoparticle concentration.

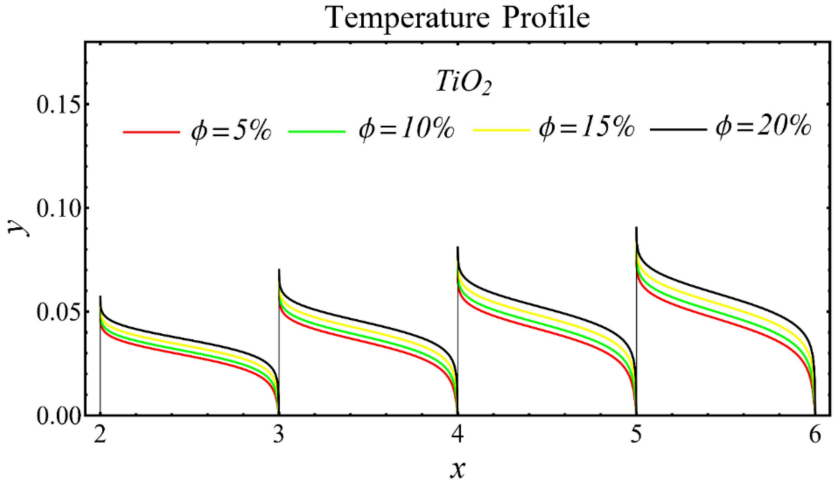

Figure 15. Temperature profile of TiO_2-EG nanofluid under influence of nanoparticle concentration.

The results of the temperature profiles for the schematic nanofluids under the influence of the nanoparticle diameter are illustrated in Figures 16–18. It is revealed that the temperature is reduced by enhancing the nanoparticle's diameter, as shown in all graphs. This is because of the increase in the Prandtl number that occurs by decreasing thermal diffusion.

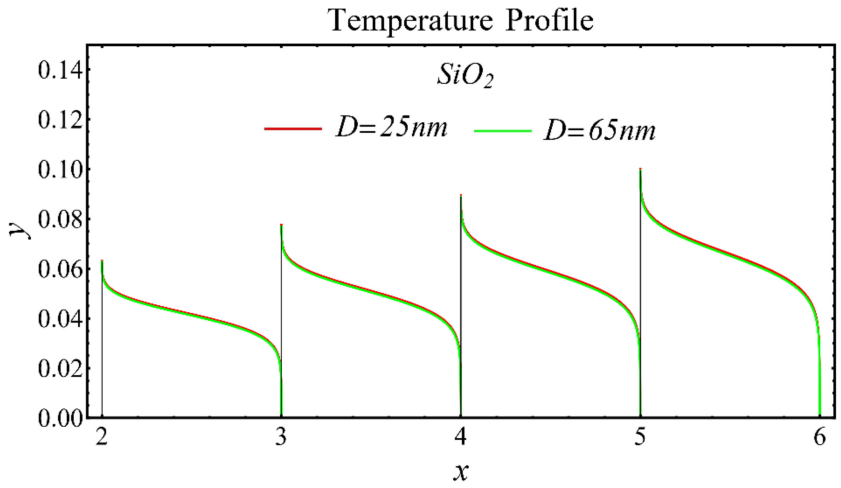

Figure 16. Temperature profile of SiO_2-EG nanofluid under influence of nanoparticle diameter.

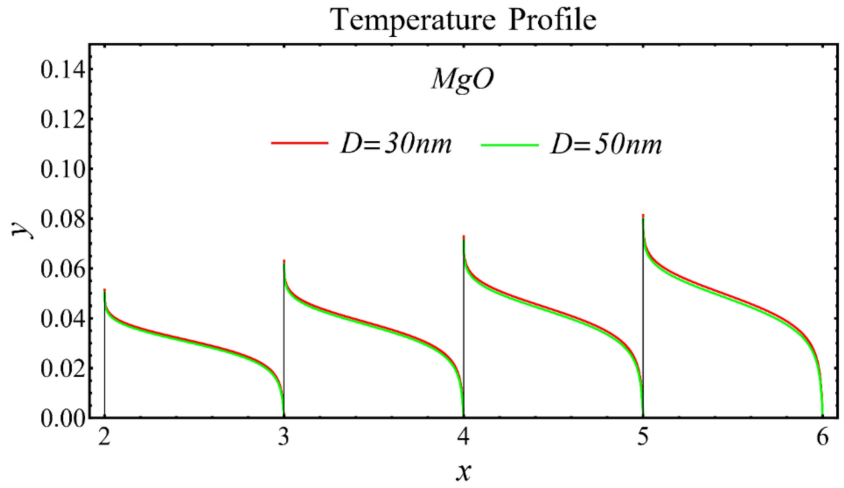

Figure 17. Temperature profile of MgO-EG nanofluid under influence of nanoparticle diameter.

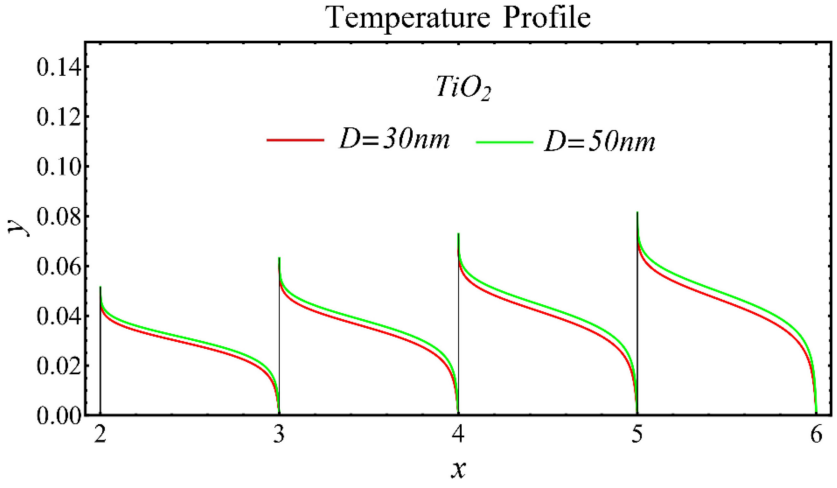

Figure 18. Temperature profile of TiO_2-EG nanofluid under influence of nanoparticle diameter.

6.3. Physical Parameters

The results of the boundary-layer parameters, such as the velocity and temperature boundary-region thicknesses, displacement thicknesses, and momentum thicknesses, are

presented in Figures 19–22, whereas the results of the coefficient of skin friction and the Nusselt number are displayed in Figures 23 and 24.

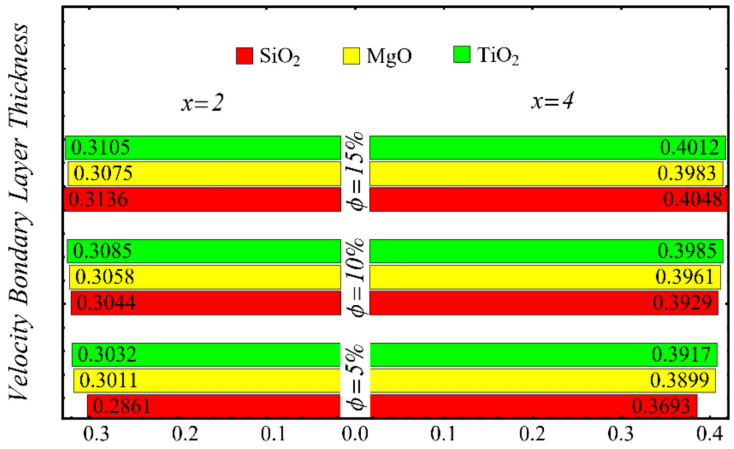

Figure 19. Velocity boundary-layer thickness at different nanoparticle concentrations.

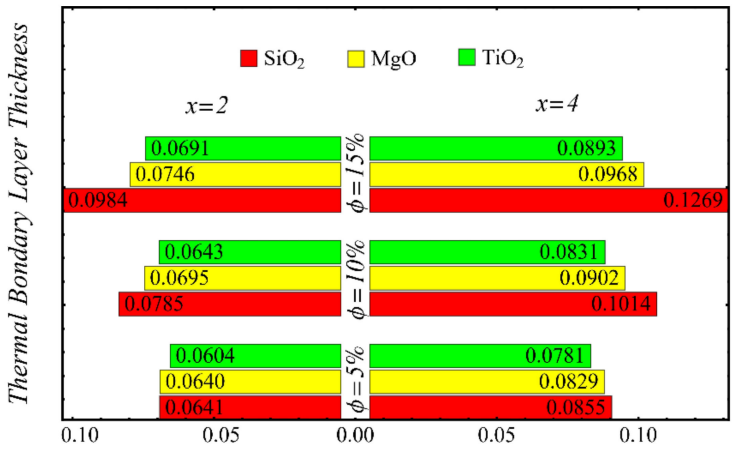

Figure 20. Temperature boundary-layer thickness at different nanoparticle concentrations.

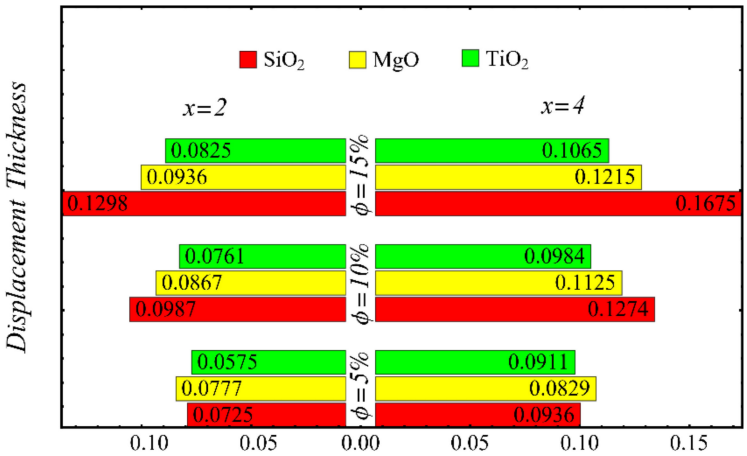

Figure 21. Displacement thickness at different nanoparticle concentrations.

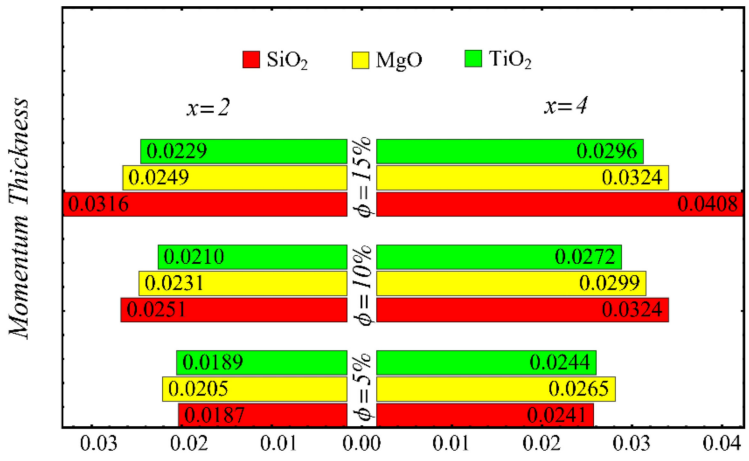

Figure 22. Momentum thickness at different nanoparticle concentrations.

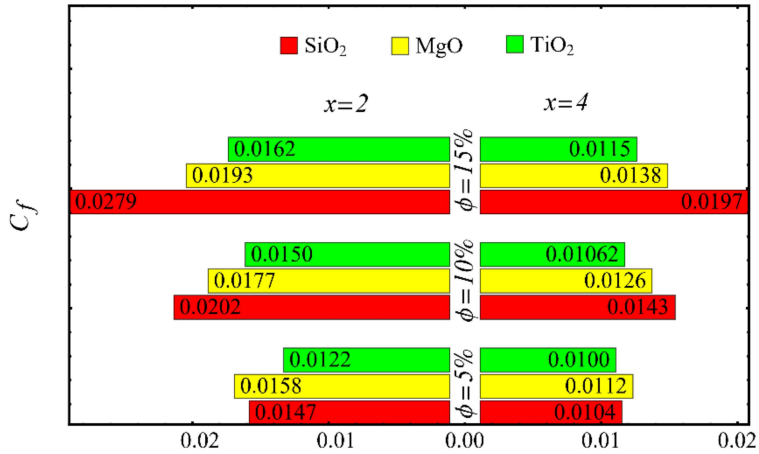

Figure 23. Coefficient of skin friction at different nanoparticle concentrations.

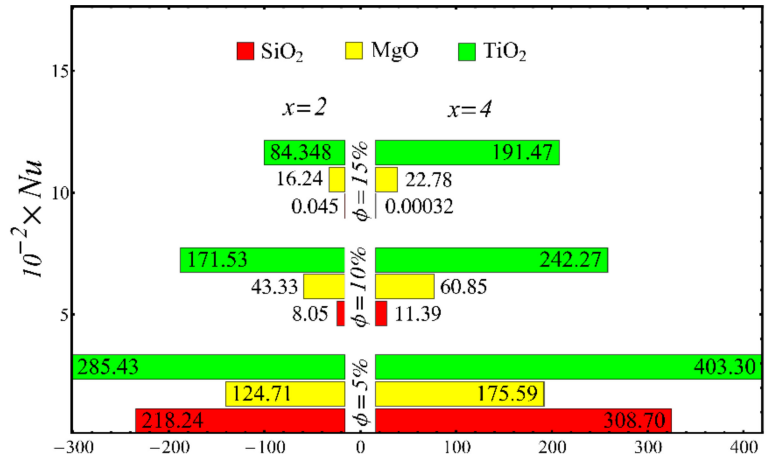

Figure 24. Nusselt number at different nanoparticle concentration.

The velocity and temperature boundary regions' thicknesses are computed at distinct positions on the surface of the wedge under the impact of nanoparticle concentrations in Figures 19 and 20. It is noted that the thickness of the velocity boundary-layer region is enlarged with the enhancement of the nanoparticle concentration and increases at a position far from the origin. It is also observed that the velocity thickness of the SiO_2-EG nanofluid is lowest at low concentrations but highest at high concentrations compared with both the MgO-EG and TiO_2-EG nanofluids. For temperature boundary-layer thickness, it is

perceived that the thickness is increased by enhancing the nanoparticle concentration. In addition, the temperature boundary-layer thickness is found to be smaller as compared with the thickness of the velocity boundary layer due to the dominant effects of mass diffusion as compared with thermal diffusion. It is further observed that the thermal boundary-layer thickness is found to be the greatest in the SiO_2-EG nanofluid as compared with both the TiO_2-EG and MgO-EG nanofluids.

Figures 21 and 22 show the results of displacement and momentum thicknesses against different nanoparticle concentrations at distinct locations on the wedge's surface. The value of the displacement thickness is raised by enhancing the nanoparticle concentration and also increases along the distance of the wedge. It is seen that the maximum displacement is found in the case of the SiO_2-EG nanofluid, and the lowest displacement is found in the TiO_2-EG nanofluid. The momentum thickness indicates a reduction in the momentum of the nanofluid, and it is observed that the value is increased by raising the nanoparticle concentration.

The values of the coefficient of skin friction for the nanofluids against the nanoparticle concentration are displayed in Figure 23. It is to be noted that the value of the coefficient of skin friction is increased when the nanoparticle concentration is enhanced, and maximum enhancement is found in the case of the SiO_2-EG nanofluid. The values of the Nusselt number with respect to the nanoparticle concentration are displayed in Figure 24. It is seen that the Nusselt number is decreased with the increase in nanoparticle concentration, and a maximum decline is found in the SiO_2-EG nanofluid as well. In addition, the trend of the results for the coefficient of skin friction and the Nusselt number agrees with the trend of published studies [55–60].

The results of the coefficient of skin friction and the Nusselt number at different values of Re_x are shown in Table 6. To calculate the results, the values of Re_x in Table 4 are used. The results show the same trend as seen in Figures 23 and 24 because Re_x is dependent on the value of the volume fraction.

Table 6. The values of C_f and Nu_x at different values of Re_x at fixed $x = 2$.

	SiO_2-EG Nanofluid D = 20−30 nm			**MgO -EG Nanofluid D = 20 nm**			**TiO_2-EG Nanofluid D = 30 nm**		
Re_x	6045	6067	6085	5448	5149	5079	5898	5847	5861
C_f	0.0147	0.0202	0.0279	0.0158	0.0177	0.0193	0.0122	0.0150	0.0162
Nu_x	218.24	8.05	0.045	124.71	43.33	16.24	285.43	171.53	84.348

7. Conclusions

In the present analysis, the boundary-layer fluid flow of three homogenous non-Newtonian nanofluids over a moving wedge is investigated. The mathematical results are presented graphically in the form of velocity and temperature profiles and further used to obtain the values of boundary-layer parameters. The main conclusions from the results are as follows:

- The profile of velocity is decreased and increased by raising the values of nanoparticle concentration and diameter, respectively.
- The profile of temperature is increased and decreased by enhancing the values of nanoparticle concentration and diameter, respectively.
- The velocity and temperature boundary-layer regions are increased by increasing the nanoparticle concentration.
- The displacement and momentum thicknesses are increased by the rise of nanoparticle concentration.
- The skin-friction coefficient is enhanced whereas the Nusselt number is decreased with the increase in nanoparticle concentration.

Author Contributions: Conceptualization, M.R., M.H. and O.D.M.; methodology, M.M.B. and M.M.; software, M.R., M.H. and O.D.M.; validation, M.M.B. and M.M.; formal analysis, M.R., M.H. and O.D.M.; investigation, M.M.B. and M.M.; resources, M.M.B. and M.M.; data curation, M.R. and M.H.; writing—original draft preparation, M.R. and M.H.; writing—review and editing, M.M.B. and M.M.; visualization, O.D.M.; supervision, M.M.B. and M.M. All authors have read and agreed to the published version of the manuscript.

Funding: This research received no external funding.

Institutional Review Board Statement: Not applicable.

Informed Consent Statement: Not applicable.

Data Availability Statement: Not applicable.

Conflicts of Interest: The authors declare no conflict of interest.

Nomenclature

u, v	Velocity components
T	Temperature of fluid
T_∞	Temperatures of inviscid region
u_∞	Velocity of fluid in inviscid region
k	Thermal conductivity
C_p	Specific heat
Ω	Wedge angle
τ	Shear stress
$\dot{\gamma}$	Shear rate
ϕ	Volume fraction
x, y	Rectangular coordinates
T_w	Temperatures of wall
ψ	Stream function
u_w	Wall velocity
ρ	Density
μ_{nf}	Consistency index
η	Similarity variable
$\mathrm{Pr}_x = \frac{\rho_{bf} c_{pbf} u_\infty x}{k_{bf} (\mathrm{Re}_x)^{\frac{2}{n-1}}}$	Local Prandtl number
$\mathrm{Re}_x = (m+1)\frac{\rho x^n}{\mu u_\infty^{n-2}}$	Local Reynold number
Subscripts	
nf	Nanofluid
np	Nanoparticle
bf	Base fluid

References

1. Yapici, K.; Osturk, O.; Uludag, Y. Dependency of nanofluid rheology on particle size and concentration of various metal oxide nanoparticles. *Braz. J. Chem. Eng.* **2018**, *35*, 575–586. [CrossRef]
2. Das, S.K.; Choi, S.U.; Yu, W.; Pradeep, T. *Nanofluids: Science and Technology*; John and Wiley and Sons: Hoboken, NJ, USA, 2007.
3. Wang, X.Q.; Mujumdar, A.S. Heat transfer characteristics of nanofluids: A review. *Int. J. Therm. Sci.* **2007**, *46*, 1–19. [CrossRef]
4. Chen, H.; Ding, Y. Heat transfer and rheological behaviour of nanofluids—A review. *Adv. Transp. Phenom.* **2009**, *1*, 135–177.
5. Nikkam, N.; Haghighi, E.B.; Saleemi, M.; Behi, M.; Khodabandeh, R.; Muhammed, M.; Palm, B.; Toprak, M.S. Experimental study on preparation and base liquid effect on thermo-physical and heat transport characteristics of α-SiC nanofluids. *Int. Commun. Heat Mass Transf.* **2014**, *55*, 38–44. [CrossRef]
6. Teja, A.S.; Beck, M.P.; Yuan, Y.; Warrier, P. The limiting behavior of the thermal conductivity of nanoparticles and nanofluids. *J. Appl. Phys.* **2010**, *107*, 114319. [CrossRef]
7. Sudeep, P.M.; Taha-Tijerina, J.; Ajayan, P.M.; Narayanan, T.N.; Anantharaman, M.R. Nanofluids based on fluorinated graphene oxide for efficient thermal management. *RSC Adv.* **2014**, *4*, 24887–24892. [CrossRef]
8. Baglioni, M.; Raudino, M.; Berti, D.; Keiderling, U.; Bordes, R.; Holmberg, K.; Baglioni, P. Nanostructured fluids from degradable nonionic surfactants for the cleaning of works of art from polymer contaminants. *Soft Matter* **2014**, *10*, 6798–6809. [CrossRef]
9. Sreeremya, T.S.; Krishnan, A.; Satapathy, L.N.; Ghosh, S. Facile synthetic strategy of oleophilic zirconia nanoparticles allows preparation of highly stable thermo-conductive coolant. *RSC Adv.* **2014**, *4*, 28020–28028. [CrossRef]

10. Cabaleiro, D.; Pastoriza-Gallego, M.J.; Gracia-Fernández, C.; Piñeiro, M.M.; Lugo, L. Rheological and volumetric properties of TiO2-ethylene glycol nanofluids. *Nanoscale Res. Lett.* **2013**, *8*, 286. [CrossRef]
11. Shima, P.D.; Philip, J. Role of thermal conductivity of dispersed nanoparticles on heat transfer properties of nanofluid. *Ind. Eng. Chem. Res.* **2014**, *53*, 980–988. [CrossRef]
12. Kole, M.; Dey, T.K. Viscosity of alumina nanoparticles dispersed in car engine coolant. *Exp. Therm. Fluid Sci.* **2010**, *34*, 677–683. [CrossRef]
13. Wen, D.; Lin, G.; Vafaei, S.; Zhang, K. Review of nanofluids for heat transfer applications. *Particuology* **2009**, *7*, 141–150. [CrossRef]
14. Rao, Y. Nanofluids: Stability, phase diagram, rheology and applications. *Particuology* **2010**, *8*, 549–555. [CrossRef]
15. Cheng, L.; Cao, D. Designing a thermo-switchable channel for nanofluidic controllable transportation. *ACS Nano* **2011**, *5*, 1102–1108. [CrossRef] [PubMed]
16. Kristiawan, B.; Rifa'i, A.I.; Enoki, K.; Wijayanta, A.T.; Miyazaki, T. Enhancing the thermal performance of TiO2/water nanofluids flowing in a helical microfin tube. *Powder Technol.* **2020**, *376*, 254–262. [CrossRef]
17. Kristiawan, B.; Wijayanta, A.T.; Enoki, K.; Miyazaki, T.; Aziz, M. Heat transfer enhancement of TiO2/water nanofluids flowing inside a square minichannel with a microfin structure: A numerical investigation. *Energies* **2019**, *12*, 3041. [CrossRef]
18. Jamshed, W.; Prakash, M.; Devi, S.; Ibrahim, R.W.; Shahzad, F.; Nisar, K.S.; Eid, M.R.; Abdel-Aty, A.H.; Khashan, M.M.; Yahia, I.S. A brief comparative examination of tangent hyperbolic hybrid nanofluid through a extending surface: Numerical Keller–Box scheme. *Sci. Rep.* **2021**, *11*, 24032. [CrossRef]
19. Reddy, M.; Rao, V.V.; Reddy, B.; Sarada, S.N.; Ramesh, L. Thermal conductivity measurements of ethylene glycol water based TiO2 nanofluids. *Nanosci. Nanotechnol. Lett.* **2012**, *4*, 105–109. [CrossRef]
20. Mariano, A.; Pastoriza-Gallego, M.J.; Lugo, L.; Camacho, A.; Canzonieri, S.; Piñeiro, M.M. Thermal conductivity, rheological behaviour and density of non-Newtonian ethylene glycol-based SnO2 nanofluids. *Fluid Phase Equilibria* **2013**, *337*, 119–124. [CrossRef]
21. Pötschke, P.; Fornes, T.D.; Paul, D.R. Rheological behavior of multiwalled carbon nanotube/polycarbonate composites. *Polymer* **2002**, *43*, 3247–3255. [CrossRef]
22. Yang, Y.; Grulke, E.A.; Zhang, Z.G.; Wu, G. Thermal and rheological properties of carbon nanotube-in-oil dispersions. *J. Appl. Phys.* **2006**, *99*, 114307. [CrossRef]
23. Seyhan, A.T.; Gojny, F.H.; Tanoğlu, M.; Schulte, K. Rheological and dynamic-mechanical behavior of carbon nanotube/vinyl ester–polyester suspensions and their nanocomposites. *Eur. Polym. J.* **2007**, *43*, 2836–2847. [CrossRef]
24. Yang, Y.; Grulke, E.A.; Zhang, Z.G.; Wu, G. Temperature effects on the rheological properties of carbon nanotube-in-oil dispersions. *Colloids Surf. A Physicochem. Eng. Asp.* **2007**, *298*, 216–224. [CrossRef]
25. Ko, G.H.; Heo, K.; Lee, K.; Kim, D.S.; Kim, C.; Sohn, Y.; Choi, M. An experimental study on the pressure drop of nanofluids containing carbon nanotubes in a horizontal tube. *Int. J. Heat Mass Transf.* **2007**, *50*, 4749–4753. [CrossRef]
26. Wang, B.; Wang, X.; Lou, W.; Hao, J. Rheological and tribological properties of ionic liquid-based nanofluids containing functionalized multi-walled carbon nanotubes. *J. Phys. Chem. C* **2010**, *114*, 8749–8754. [CrossRef]
27. Phuoc, T.X.; Massoudi, M.; Chen, R.H. Viscosity and thermal conductivity of nanofluids containing multi-walled carbon nanotubes stabilized by chitosan. *Int. J. Therm. Sci.* **2011**, *50*, 12–18. [CrossRef]
28. Ruan, B.; Jacobi, A.M. Ultrasonication effects on thermal and rheological properties of carbon nanotube suspensions. *Nanoscale Res. Lett.* **2012**, *7*, 127. [CrossRef]
29. Wang, J.; Zhu, J.; Zhang, X.; Chen, Y. Heat transfer and pressure drop of nanofluids containing carbon nanotubes in laminar flows. *Exp. Therm. Fluid Sci.* **2013**, *44*, 716–721. [CrossRef]
30. Shahid, A.; Bhatti, M.M.; Ellahi, R.; Mekheimer, K.S. Numerical experiment to examine activation energy and bi-convection Carreau nanofluid flow on an upper paraboloid porous surface: Application in solar energy. *Sustain. Energy Technol. Assess.* **2022**, *52*, 102029. [CrossRef]
31. Tseng, W.J.; Lin, K.C. Rheology and colloidal structure of aqueous TiO2 nanoparticle suspensions. *Mater. Sci. Eng. A* **2003**, *355*, 186–192. [CrossRef]
32. He, Y.; Jin, Y.; Chen, H.; Ding, Y.; Cang, D.; Lu, H. Heat transfer and flow behaviour of aqueous suspensions of TiO2 nanoparticles (nanofluids) flowing upward through a vertical pipe. *Int. J. Heat Mass Transf.* **2007**, *50*, 2272–2281. [CrossRef]
33. Chen, H.; Yang, W.; He, Y.; Ding, Y.; Zhang, L.; Tan, C.; Lapkin, A.A.; Bavykin, D.V. Heat transfer and flow behaviour of aqueous suspensions of titanate nanotubes (nanofluids). *Powder Technol.* **2008**, *183*, 63–72. [CrossRef]
34. Chen, H.; Witharana, S.; Jin, Y.; Kim, C.; Ding, Y. Predicting thermal conductivity of liquid suspensions of nanoparticles (nanofluids) based on rheology. *Particuology* **2009**, *7*, 151–157. [CrossRef]
35. Bobbo, S.; Fedele, L.; Benetti, A.; Colla, L.; Fabrizio, M.; Pagura, C.; Barison, S. Viscosity of water based SWCNH and TiO2 nanofluids. *Exp. Therm. Fluid Sci.* **2012**, *36*, 65–71. [CrossRef]
36. Penkavova, V.; Tihon, J.; Wein, O. Stability and rheology of dilute TiO2-water nanofluids. *Nanoscale Res. Lett.* **2011**, *6*, 273. [CrossRef] [PubMed]
37. Chevalier, J.; Tillement, O.; Ayela, F. Rheological properties of nanofluids flowing through microchannels. *Appl. Phys. Lett.* **2007**, *91*, 233103. [CrossRef]
38. Tavman, I.; Turgut, A.; Chirtoc, M.; Schuchmann, H.P.; Tavman, S. Experimental investigation of viscosity and thermal conductivity of suspensions containing nanosized ceramic particles. *Arch. Mater. Sci.* **2008**, *100*, 99–104.

39. Chevalier, J.; Tillement, O.; Ayela, F. Structure and rheology of SiO 2 nanoparticle suspensions under very high shear rates. *Phys. Rev. E* **2009**, *80*, 051403. [CrossRef]
40. Jung, Y.; Son, Y.H.; Lee, J.K.; Phuoc, T.X.; Soong, Y.; Chyu, M.K. Rheological behavior of clay–nanoparticle hybrid-added bentonite suspensions: Specific role of hybrid additives on the gelation of clay-based fluids. *ACS Appl. Mater. Interfaces* **2011**, *3*, 3515–3522. [CrossRef]
41. Mondragon, R.; Julia, J.E.; Barba, A.; Jarque, J.C. Determination of the packing fraction of silica nanoparticles from the rheological and viscoelastic measurements of nanofluids. *Chem. Eng. Sci.* **2012**, *80*, 119–127. [CrossRef]
42. Anoop, K.; Sadr, R.; Al-Jubouri, M.; Amani, M. Rheology of mineral oil-SiO2 nanofluids at high pressure and high temperatures. *Int. J. Therm. Sci.* **2014**, *77*, 108–115. [CrossRef]
43. Żyła, G.; Cholewa, M.; Witek, A. Rheological properties of diethylene glycol-based MgAl 2 O 4 nanofluids. *RSC Adv.* **2013**, *3*, 6429–6434. [CrossRef]
44. Mostafizur, R.M.; Aziz, A.A.; Saidur, R.; Bhuiyan, M.H.U.; Mahbubul, I.M. Effect of temperature and volume fraction on rheology of methanol based nanofluids. *Int. J. Heat Mass Transf.* **2014**, *77*, 765–769. [CrossRef]
45. Hojjat, M.; Etemad, S.G.; Bagheri, R.; Thibault, J. Rheological characteristics of non-Newtonian nanofluids: Experimental investigation. *Int. Commun. Heat Mass Transf.* **2011**, *38*, 144–148. [CrossRef]
46. Chen, H.; Ding, Y.; Lapkin, A. Rheological behaviour of nanofluids containing tube/rod-like nanoparticles. *Powder Technol.* **2009**, *194*, 132–141. [CrossRef]
47. Lu, K. Rheological behavior of carbon nanotube-alumina nanoparticle dispersion systems. *Powder Technol.* **2007**, *177*, 154–161. [CrossRef]
48. Chen, H.; Ding, Y.; Tan, C. Rheological behaviour of nanofluids. *New J. Phys.* **2007**, *9*, 367. [CrossRef]
49. Chhabra, R.P.; Richardson, J.F. *Non-Newtonian Flow and Applied Rheology: Engineering Applications*; Butterworth-Heinemann: Oxford, UK, 2011.
50. Mahian, O.; Kolsi, L.; Amani, M.; Estellé, P.; Ahmadi, G.; Kleinstreuer, C.; Marshall, J.S.; Siavashi, M.; Taylor, R.A.; Niazmand, H.; et al. Recent advances in modeling and simulation of nanofluid flows-Part I: Fundamentals and theory. *Phys. Rep.* **2019**, *790*, 1–48. [CrossRef]
51. Bhatti, M.M.; Bég, O.A.; Abdelsalam, S.I. Computational Framework of Magnetized MgO–Ni/Water-Based Stagnation Nanoflow Past an Elastic Stretching Surface: Application in Solar Energy Coatings. *Nanomaterials* **2022**, *12*, 1049. [CrossRef]
52. Zhang, L.; Bhatti, M.M.; Michaelides, E.E.; Marin, M.; Ellahi, R. Hybrid nanofluid flow towards an elastic surface with tantalum and nickel nanoparticles, under the influence of an induced magnetic field. *Eur. Phys. J. Spec. Top.* **2021**, 1–13. [CrossRef]
53. Yacob, N.A.; Ishak, A.; Pop, I. Falkner–Skan problem for a static or moving wedge in nanofluids. *Int. J. Therm. Sci.* **2011**, *50*, 133–139. [CrossRef]
54. Kuo, B.L. Heat transfer analysis for the Falkner–Skan wedge flow by the differential transformation method. *Int. J. Heat Mass Transf.* **2005**, *48*, 5036–5046. [CrossRef]
55. Reddy, P.S.; Sreedevi, P. Effect of thermal radiation and volume fraction on carbon nanotubes based nanofluid flow inside a square chamber. *Alex. Eng. J.* **2021**, *60*, 1807–1817. [CrossRef]
56. Marzougui, S.; Mebarek-Oudina, F.; Assia, A.; Magherbi, M.; Shah, Z.; Ramesh, K. Entropy generation on magneto-convective flow of copper–water nanofluid in a cavity with chamfers. *J. Therm. Anal. Calorim.* **2021**, *143*, 2203–2214. [CrossRef]
57. Gul, T.; Bilal, M.; Alghamdi, W.; Asjad, M.I.; Abdeljawad, T. Hybrid nanofluid flow within the conical gap between the cone and the surface of a rotating disk. *Sci. Rep.* **2021**, *11*, 1180. [CrossRef]
58. Khan, U.; Ahmed, N.; Mohyud-Din, S.T.; Hamadneh, N.N.; Khan, I.; Andualem, M. The dynamics of H2O suspended by multiple Shaped Cu nanoadditives in rotating system. *J. Nanomater.* **2021**, *2021*, 7299143. [CrossRef]
59. Jamshed, W.; Eid, M.R.; Aissa, A.; Mourad, A.; Nisar, K.S.; Shahzad, F.; Saleel, C.A.; Vijayakumar, V. Partial velocity slip effect on working magneto non-Newtonian nanofluids flow in solar collectors subject to change viscosity and thermal conductivity with temperature. *PLoS ONE* **2021**, *16*, e0259881. [CrossRef]
60. Ali Zaidi, S.Z.; Khan, U.; Abdeljawad, T.; Ahmed, N.; Mohyud-Din, S.T.; Khan, I.; Nisar, K.S. Investigation of thermal transport in multi-Shaped Cu nanomaterial-based nanofluids. *Materials* **2020**, *13*, 2737.